NANO LETTERS

Letter

pubs.acs.org/NanoLett

Strain Engineering of Kapitza Resistance in Few-Layer Graphene

Jie Chen,[†] Jens H. Walther,[†,‡] and Petros Koumoutsakos*[,†]

[†]Computational Science and Engineering Laboratory, Department of Mechanical and Process Engineering, ETH Zurich, CH-8092 Zurich, Switzerland

[‡]Department of Mechanical Engineering, Technical University of Denmark, DK-2800 Kgs. Lyngby, Denmark

Supporting Information

ABSTRACT: We demonstrate through molecular dynamics simulations that the Kapitza resistance in few-layer graphene (FLG) can be controlled by applying mechanical strain. For unstrained FLG, the Kapitza resistance decreases with the increase of thickness and reaches an asymptotic value of 6×10^{-10} m^{2}K/W at a thickness about 16 nm. Uniaxial cross-plane strain is found to increase the Kapitza resistance in FLG monotonically, when the applied strain varies from compressive to tensile. Moreover, uniaxial strain couples the in-plane and out-of-plane strain/stress when the surface of FLG is buckled. We find that with a compressive cross-plane stress of 2 GPa, the Kapitza resistance is reduced by about 50%. On the other hand it is almost tripled with a tensile cross-plane stress of 1 GPa. Remarkably, compressive in-plane strain can either increase or reduce the Kapitza resistance, depending on the specific way it is applied. Our study suggests that graphene can be exploited for both heat dissipation and insulation through strain engineering.

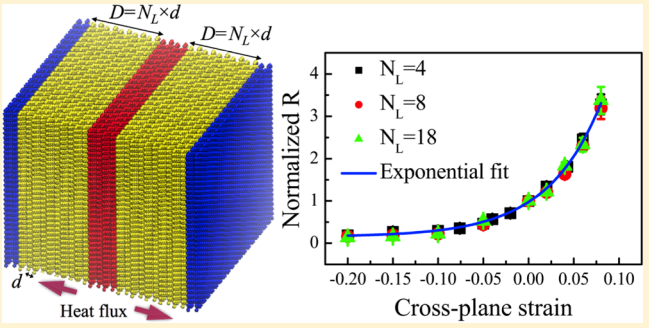

KEYWORDS: *Strain effect, Kapitza resistance, few-layer graphene, molecular dynamics simulations, vibrational density of states*

The high in-plane thermal conductivity of graphene[1,2] makes it a promising material for high-efficiency heat dissipation devices.[3−6] The thermal conductivity of suspended single-layer graphene (SLG) at room temperature has been found experimentally to reach a high value ∼2500−5300 W/m-K.[7−9] Moreover, measurements of the temperature-dependent phonon transport in suspended SLG have been reported in experimental studies.[10] For suspended few-layer graphene (FLG), the in-plane thermal conductivity is lower[11−13] and decreases with the number of layers, converging after a few atomic layers to that of graphite ∼1000−2000 W/m-K.[11]

Remarkably, FLG can also serve as a heat insulator, as its cross-plane thermal conductivity is more than 2 orders of magnitude smaller than the in-plane thermal conductivity.[3] Recent experimental study on FLG with thickness ∼35 nm reported the cross-plane thermal conductivity ∼0.7 W/m-K at room temperature.[14] Further reduction of the cross-plane thermal conductivity to the amorphous limit is desirable for heat insulation applications. In this regard, tuning the interfacial thermal resistance (i.e., Kapitza resistance) between graphene sheets and therefore controlling cross-plane heat transport is a key toward the design of graphene-based device for heat dissipation and insulation.

Strain engineering is a versatile tool to tailor the physical properties of graphene.[15−20] For instance, the thermal conductivity of suspended SLG can be reduced by both compressive and tensile strain.[18] Recent first-principles calculations have shown that strain has significant impact on the acoustic phonon lifetimes in suspended SLG.[19] However, only in-plane strain and its effect on in-plane heat transport in graphene has been considered in these studies.

In this Letter, we systematically study the Kapitza resistance in both unstrained and uniaxially strained FLG for the first time by using molecular dynamics (MD) simulations. The effects of both cross-plane and in-plane strain on Kapitza resistance are studied and the underlying physical mechanism is discussed. Our study provides practical guidance to experiments for the engineering of Kapitza resistance in FLG by uniaxial strain.

All MD simulations in our study are performed by using LAMMPS package.[21] Optimized Tersoff potential[22] for graphene is used to model the C−C bond within the same graphene sheet, while Lennard-Jones (LJ) potential $V(r_{ij}) = 4\varepsilon[(\sigma/r_{ij})^{12} - (\sigma/r_{ij})^{6}]$ with optimized parameters for graphene[23] is used to model the interlayer C−C interactions between different layers. The cutoff distance of LJ potential is set as 2.5σ. Moreover, the neighbor list is updated every ten time steps, and each time step is set as 0.2 fs in our simulations.

Nonequilibrium molecular dynamics (NEMD) simulations are used to calculate the Kapitza resistance of graphene, as shown in Figure 1. In the present study, we consider square graphene sheets with cross section of $L \times L$ and interlayer distance d. Periodic boundary condidtions are used in all directions. Nosé-Hoover heat bath is used to simulate the heat

Received: November 11, 2013
Revised: January 10, 2014
Published: January 15, 2014

   dx.doi.org/10.1021/nl404182k | *Nano Lett.* 2014, 14, 819−825

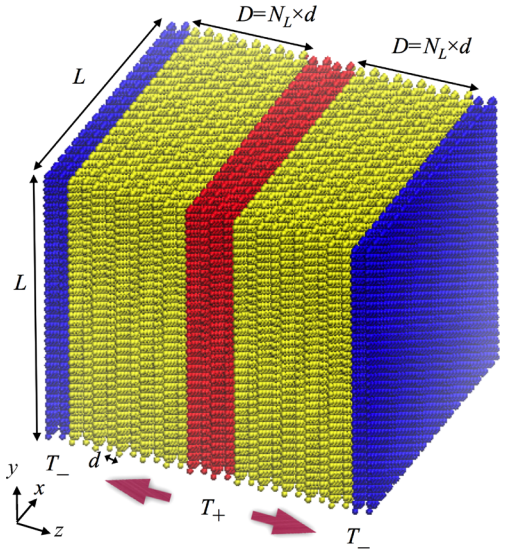

Figure 1. Schematic setup of the nonequilibrium molecular dynamics simulations. The graphene sheets have cross sectional size $L \times L$, and interlayer distance d. The heat bath with high temperature T_+ and low temperature T_- is applied to the center (red) and two ends (blue), respectively. Periodic boundary conditions are applied in all directions. Heat flows in two directions from T_+ to T_-. Between two heat baths, there are N_L layers of graphene (yellow) at each side. In-plane directions are in XY plane, and the cross-plane direction is in the z-axis.

source and sink at different temperature. There are N_L layers of graphene between the heat source and sink. The heat flux J is defined as the energy injected into/removed from the heat source/sink across unit area per unit time.[24] The Kapitza resistance is calculated based on a linear regression analysis of the temperature profile. More details about the simulations and calculations are presented in Supporting Information.

We first systematically study the Kapitza resistance R in unstrained graphene. The graphene sheets are thermally equilibrated at room temperature with the isothermal−isobaric (NPT) ensemble and all stress components are fully relaxed (Supporting Information Figure S1a). NEMD simulations with the canonical (NVT) ensemble are then applied to the unstrained graphene sheets to calculate R. The previous study[25] has examined configurations at very small L. We find that R is dependent on L when the cross section is small. Hence we perform a convergence study on four layers of graphene for R at different L to identify the minimum size of the graphene cross section for which edge and chirality effect will be negligible. Our simulations indicate that R remains constant for $L \geq 8$ nm (Figure 2a). For four layers of graphene with $L = 8$ nm, we find $R \approx 3.82 \times 10^{-9}$ m^{2}K/W. Using the same setup, we also test the force field in ref 26 on four layers of graphene with $L = 8$ nm, and find $R \approx 4.46 \times 10^{-9}$ m^{2}K/W. Thus we choose $L \geq 8$ nm and extend to study the effect of layer number N_L on Kapitza resistance. We find R is indistinguishable between $L = 8$ nm and $L = 10$ nm for different N_L (Figure 2b). Moreover, R decreases asymtotically with the increase of N_L toward a constant value $\sim 6 \times 10^{-10}$ m^{2}K/W at 48 layers (thickness ~16 nm). This asymptotic value is in close agreement with recent results on room temperature Kapitza resistance of graphene from theoretical study using first principles calculations ($\sim 6 \times 10^{-10}$ m^{2}K/W)[27] and experimental study based on X-ray diffraction measurements ($\sim 5 \times 10^{-10}$ m^{2}K/W).[14] It is also consistent with previous MD

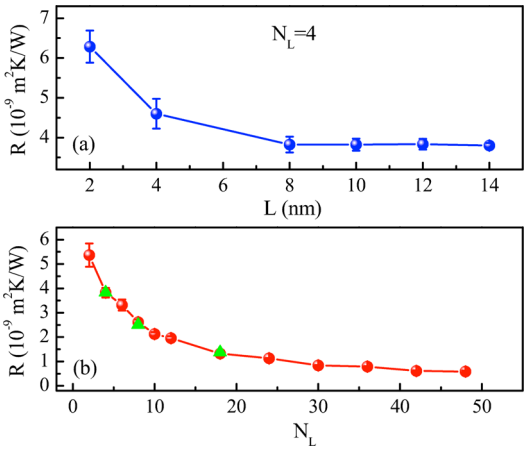

Figure 2. Kapitza resistance R in unstrained graphene at room temperature. (a) R versus cross sectional size L for 4 layers of graphene. (b) R versus number of graphene layers N_L with fixed cross sectional size $L = 8$ nm (circle) and $L = 10$ nm (triangle).

simulation results.[25] The results for unstrained graphene validate the accuracy of our simulations, and serve as the control system for the study of the strain effect on Kapitza resistance in the following part.

To study the strain effect on cross-plane heat transport in FLG, we apply uniaxial strain to the graphene sheets after thermal equilibration. The strain is defined as $e = (l - l_0)/l_0$, where l_0 and l are the length of the simulation box in the strain loading direction for the unstrained and strained graphene, respectively. Uniaxial strain is applied in the specified direction by deforming the size of the simulation domain in the strain loading direction at a constant strain rate,[28] while keeping the size of the plane perpendicular to the strain loading direction fixed (NVT ensemble).

We first study the effect of uniaxial strain along the heat transport direction. Figure 3 shows the strain−stress relation in FLG under uniaxial cross-plane strain e_c. When compressive e_c is applied, the cross-plane stress P_{zz} increases monotonically, while there is no stress in the in-plane directions (Figure 3a). We have verified that this strain−stress relation is independent of the strain rate and the system size used in our simulations (Supporting Information Figure S4). Moreover, the total energy E_t increases with the increase of e_c, while the standard deviation of the z-coordinate S_z (see Supporting Information for calculation details) decreases (Figure 3b). Consequently, the graphene sheets does not exhibit any large deformation (Supporting Information Figure S7a).

When the tensile e_c is applied, P_{zz} increases monotonically until a critical strain $e_c \sim 0.1$ (Figure 3c). This critical strain has a very weak dependence on the simulation parameters (Supporting Information Figure S5). Interestingly, we find an interplay between cross-plane strain and in-plane stress; a nonzero in-plane stress starts to accumulate when the tensile cross-plane strain is larger than a certain threshold (~4%). This is because the LJ interaction between graphene sheets is weakened due to the increased interlayer distance by tensile e_c (Supporting Information Figure S10), as indicated by the increase of total energy (Figure 3d). Because of this suppressed interlayer interaction, the out-of-plane vibration increases quite significantly compared to that in the unstrained graphene (Figure 3d). For instance, at 8% tensile e_c, S_z is about one order of magtitude larger than that in unstrained graphene. This

dx.doi.org/10.1021/nl404182k | Nano Lett. 2014, 14, 819−825

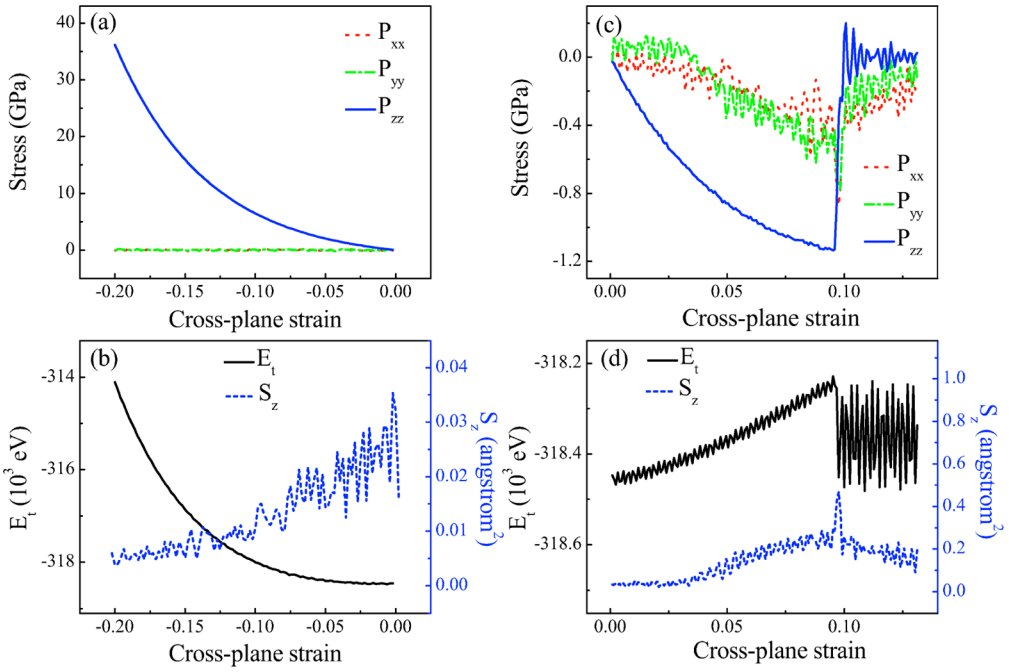

Figure 3. Strain–stress relation, total energy E_t, and standard deviation of z-coordinate S_z versus uniaxial cross-plane strain in few-layer graphene. The uniaxial strain is applied in the z-direction. (a,b) Compressive cross-plane strain. (c,d) Tensile cross-plane strain.

enhanced out-of-plane motion causes the so-called "buckling phenomenon"[18] in graphene (Supporting Information Figure S7). When e_c is larger than the critical strain ~0.1, FLG breaks up because the applied tensile strain overcomes the interlayer LJ potential, as revealed by the sudden change of total energy (Figure 3d), thus releasing all the stress components. Correspondingly, S_z is reduced after the critical strain. Compared to the same amount of compressive cross-plane strain, the variations of both stress and total energy induced by tensile cross-plane strain are much smaller.

The Kapitza resistance at room temperature in FLG under various e_c is shown in Figure 4a. Compressive e_c is found to reduce R, while the tensile e_c leads to the increase of R. When e_c varies from compressive to tensile, R increases monotonically, showing an exponential correlation with the variation of e_c (lines in Figure 4a). More interestingly, we find the relative variation of R, which is normalized by R in unstrained graphene at each N_L, follows the same exponential dependence on e_c, regardless of the thickness. Moreover, our simulation results show that with 5% compressive e_c, which induces a stress ~2 GPa, R can be reduced by 50%. In Figure 3, the maximum stress induced by cross-plane strain is less than 40 GPa, which is much lower than the extreme stress of graphene ~130 GPa measured in experiment.[29] On the other hand, we find that R is almost tripled with 7% tensile e_c, which induces a stress ~1 GPa. In this case, we estimate the corresponding cross-plane thermal conductivity based on the asymptotic value $\sim 6 \times 10^{-10}$ m^2K/W and interlayer distance d = 3.4 Å for the unstrained graphene. We find a very low thermal conductivity ~0.2 W/m-K, which is close to that for the amorphous limit of carbon film.[30] Our study suggests that graphene can be used for both thermal dissipation and insulation through strain engineering.

The vibrational density of states[31,32] (DOS) can provide further insights into the heat transfer mechanism in both unstrained and strained FLG (see Supporting Information for calculation details). For the unstrained FLG, the characteristic G-peak of graphene at ~1600 cm^{-1} (~48 THz)[33,34] is well

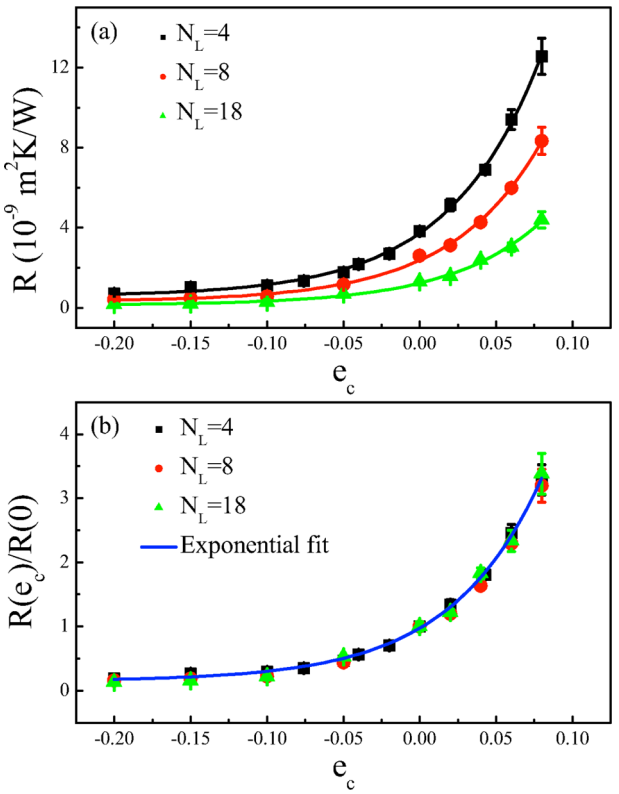

Figure 4. Room-temperature Kapitza resistance R in few-layer graphene versus uniaxial cross-plane strain e_c. Symbols denote raw data for different number of graphene layers N_L, and lines draw the exponential fit to the raw data according to $y = y_0 + A \exp(e_c/B)$, where y_0, A, and B are the fitting parameters. (a) Absolute value. (b) Relative value normalized by Kapitza resitance in unstrained graphene with y_0 = 0.151 ± 0.025, A = 0.825 ± 0.034, and B = 0.060 ± 0.002.

reproduced by our calculations (Figure 5a). Moreover, the total DOS of strained FLG exhibits a blue/red shift for low-

dx.doi.org/10.1021/nl404182k | Nano Lett. 2014, 14, 819–825

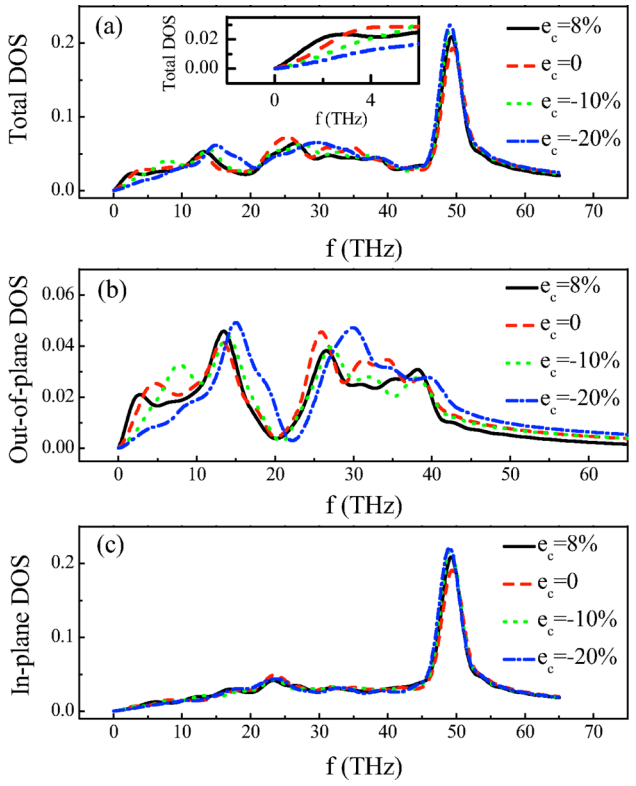

Figure 5. Vibrational DOS of few-layer graphene under different uniaxial cross-plane strain e_c. (a) Total DOS. The inset zooms in for the low-frequency phonons. (b) DOS for out-of-plane vibration. (c) DOS for in-plane vibration.

frequency phonons near the Brillouin zone center when subjected to compressive/tensile e_c. However, the G-peak is almost unaffected by e_c. Qualitatively similar effects on phonon spectrum induced by strain have been reported in different material systems.[18,35,36] The polarized DOS further reveals that the frequency shift of the zone-center phonons (less than 4 THz) induced by e_c stems from the low-frequency out-of-plane vibration (Figure 5b), corresponding to the flexual acoustic (ZA) phonons.[33] In contrast, DOS for in-plane phonons is independent of e_c (Figure 5c).

This frequency shift of ZA phonons can be understood from the strength of interlayer interaction in FLG. For unstrained FLG, the system is in the lowest-energy configuration, that is, at the valley of LJ potential (Supporting Information Figure S10a). With the application of compressive e_c, the system is driven away from the global minimum so the total energy increases (Figure 3b). This leads to the increase of the harmonic force constant in LJ potential (Supporting Information Figure S10b) so that interlayer interactions become more stiff, as demonstrated by the suppressed bending of graphene surface (Figure 3b). The enhanced harmonic force constant increases the phonon frequency, thus causing the blue shift of ZA phonons. Similarly, the tensile cross-plane strain drives the system away from the global minimum to the opposite direction, causing the softening of interlayer interaction (Supporting Information Figure S10b) and enhanced buckling effect (Figure 3d), and thus leads to the red shift of ZA phonons.

Along the heat transport direction, the interlayer interaction in FLG is a weak interaction compared to the intralayer convalent bonding. For weakly coupled systems, previous theoretical investigations on lattice models have found that the heat flux across the interface is proportional to the square of interfacial coupling strength.[37,38] Hence Kapitza resistance at the weakly coupled interface can be tuned by the coupling strength. Similar effect on Kapitza resistance has also been found in realistic material systems.[31,39] The compressive/tensile e_c results in the stiffening/softening of the interlayer interaction

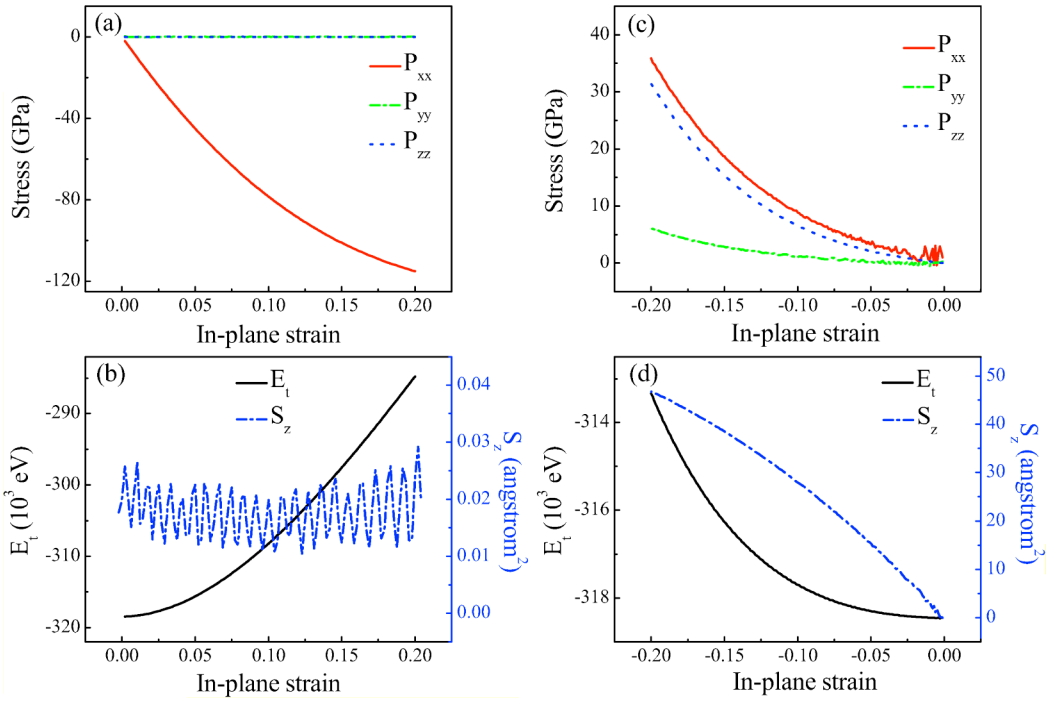

Figure 6. Strain−stress relation, total energy E_t, and standard deviation of z-coordinate S_z versus uniaxial in-plane strain in few-layer graphene. The uniaxial strain is applied in the x-direction. (a,b) Tensile in-plane strain. (c,d) Compressive in-plane strain.

dx.doi.org/10.1021/nl404182k | Nano Lett. 2014, 14, 819−825

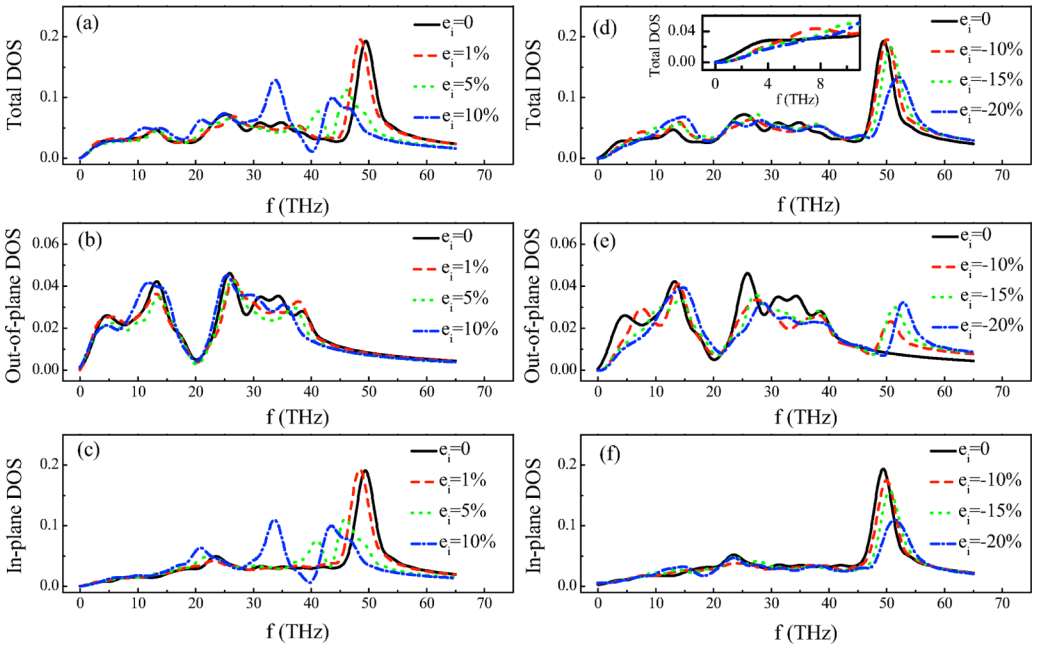

Figure 7. Vibrational DOS of few-layer graphene under different uniaxial in-plane strain e_i. (a–c) Tensile in-plane strain. (d–f) Compressive in-plane strain. The inset zooms in for the low-frequency phonons.

strength in FLG, thus leading to the decrease/increase of Kapitza resistance shown in Figure 4.

The strain effect on Kapitza resistance in FLG can also be understood from the kinetic theory in which thermal conductivity of a solid can be expressed as $\kappa = \sum_\lambda C_\lambda v_\lambda l_\lambda$. Here $\lambda(\mathbf{k},p)$ is the phonon mode index, depending on wavevector $\mathbf{k}$ and polarization p. C, v, and l denotes specific heat, group velocity, and mean-free path of each phonon mode, respectively. Using lattice dynamics calculations, Li et al. studied the effect of strain on phonon dispersion relation for bulk silicon and diamond.[18] They found compressive/tensile strain causes the blue/red shift of phonon spectrum, which is consistent with our MD simulation results. Such frequency shift of the phonon spectrum induced by compressive/tensile strain results in the increase/decrease of both phonon group velocity and specific heat, thus leading to the increase/decrease of thermal conducitivty.[18] The Kapitza resistance R of FLG is related to the cross-plane thermal conductivity κ as $R = d/\kappa$, where d is the interlayer distance. Since the compressive/tensile e_c causes the decrease/increase of d and increase/decrease of κ, R is reduced/increased consequently.

Most theoretical and experimental works[18,19,35,36] have considered strain effect in SLG, where only in-plane strain is relavant. Therefore, it is important to understand how the phonon spectrum in FLG depends on the in-plane strain/stress, and how the in-plane strain affects the cross-plane heat transport in such a quasi-2D system. In this regard, we extend our study to the effect of in-plane strain on Kapitza resistance in FLG.

Figure 6 shows the strain–stress relation in FLG under uniaxial in-plane strain. Similar to the cross-plane strain, the in-plane strain e_i causes the increase of system energy. When tensile e_i is applied uniaxially in the x-direction, the in-plane stress P_{xx} increases monotonically with the increase of e_i, while the stress in the other two directions remains zero, regardless of e_i. Moreover, S_z in FLG under tensile e_i is almost the same as that for the unstrained counterpart (Figure 6b). The buckling phenomenon does not occur in this case (Supporting Information Figure S7c). In contrast, the compressive e_i not only results in the increase of stress in the strain-loading direction, it also induces the increase of both stress components in the plane that is perpendicular to the strain-loading direction (Figure 6c), in particular for the cross-plane stress. This demonstrates that there exists a coupling between in-plane strain and cross-plane stress. Furthermore, S_z increases significantly with the increase of compressive e_i (Figure 6d), and the surface of FLG is obviously buckled (Supporting Information Figure S7d). Combining results for the cross-plane strain (Figure 3), we find that the coupling between in-plane and cross-plane strain/stress in FLG only exists when the buckling phenomenon takes place.

We notice that a quite large amount of cross-plane stress is induced by the compressive e_i during uniaxial strain-loading. We perform additional simulations in which e_i is loaded in the x-direction while the simulation box size of the other two directions is allowed to deform (NPT ensemble) in order to achieve zero stress. These additional simulations are referred as the "reference system" in this paper.

Figure 7 shows the DOS for FLG under uniaxial e_i. With a small amount of tensile e_i, the G-peak shifts to the lower frequency (Figure 7a). With the increase of tensile e_i, red shift of G-peak becomes larger, and the G-peak splits into two peaks due to the breaking of the double-degeneracy of the in-plane phonons.[33] This trend is qualitatively in good agreement with Raman measurement of SLG under tensile in-plane strain.[35] We note that the applied strain in our simulation is larger compared to the experimental values. Presumably this is due to the much larger sample size of graphene on the order of 10 μm used in experiment,[35] compared to the typical sample size on the order of 10 nm used in our simulation. Furthermore, we find the tensile e_i mainly affects the in-plane phonon spectrum (Figure 7c) but has neglibible impact on the out-of-plane phonon spectrum (Figure 7b). This is because the cross-plane

dx.doi.org/10.1021/nl404182k | Nano Lett. 2014, 14, 819–825

stress that affects the out-of-plane phonon spectrum is decoupled from the tensile in-plane strain (Figure 6a).

When compressive e_i is applied, the G-peak shifts to higher frequency continuously with the increase of compressive e_i (Figure 7d), but the frequency shift is much smaller compared to that with the same amount of tensile e_i, consistent with previous experimental study.[36] This result also explains why the in-plane DOS is insensitive to tensile e_c (Figure 5c) despite the existing coupling between in-plane and cross-plane strain/stress. We find from our simulation that 10% compressive e_i, inducing in-plane stress of ~10 GPa, only results in ~0.6 THz blue shift of the G-peak. With tensile e_c, the maximum induced in-plane stress is less than 1 GPa (Figure 3c). In this case, the resultant frequency shift is too small compared to the width of the G-peak thus cannot be detected in our simulation. Furthermore, the cross-plane stress induced by the compressive e_i results in the blue shift of the zone-center ZA phonons (Figure 7e). More interestingly, the G-peak, which is a charactistic of the in-plane phonons,[33] also appears in the out-of-plane phonon spectrum when FLG is under large compressive e_i, suggesting a mixing effect of in-plane and out-of-plane phonon spectrum. In the reference system without the cross-plane stress, the frequency shift of ZA phonons disappears but the mixing effect of phonon spectrum still exists (Supporting Information Figure S9b). In contrast, this mixing effect does not occur in unstrained FLG or FLG under cross-plane strain (Figure 5b). This is because when FLG is under compressive in-plane strain, the surface is seriously buckled (Supporting Information Figure S7d). For instance, with 10% compressive e_i, S_z is about 3 orders of magnitude larger than that in unstrained graphene (Figure 6d). In contrast to the almost flat surface in unstrained graphene, the severely bended graphene surface causes a strong coupling between in-plane and out-of-plane vibration, thus leading to the mixing of phonon spectrum.

The phonon spectrum analysis elucidates how in-plane strain can be used to control cross-plane vibration. To further assess the impact of in-plane strain on cross-plane thermal transport, we finally calculate the Kapitza resistance R in FLG under in-plane strain. Figure 8 shows R in four layers of graphene under different e_i at room temperature. The variation of cross sectional area caused by the in-plane strain has been taken into account in the calculation of R. It is found that the tensile e_i has negligible impact on R, as the out-of-plane vibration is not affected by the tensile in-plane strain (Figure 7b). With compressive e_i, in the reference system without cross-plane stress R increases and saturates at large compressive e_i due to the saturation of in-plane stress (Supporting Information Figure S8a). This is because the largely deformed graphene surface, induced by the compressive e_i, enhances the surface scattering of phonons and thus suppresses the heat transport.[18] On the other hand, uniaxial compressive e_i also induces blue shift of ZA phonons (Figure 7e) that can reduce Kapitza resistance (Figure 4). Therefore, R in FLG under uniaxial compressive e_i is determined by these two competing factors. At small uniaxial compressive e_i, the induced cross-plane stress is very small so enhanced surface scattering is the dominating factor. As a result, R is larger than that of the unstrained counterpart. With the increase of uniaxial compressive e_i, the cross-plane stress increases monotonically so that the shift of phonon spectrum becomes dominating, leading to the monotonic decrease of R. These results not only provide practical guidance to experiments that in-plane strain can be used to tune Kapitza resistance of FLG, depending on the specific way how the in-plane strain is applied, but also have important implications for simulations. If the structure of graphene is not properly relaxed before thermal characterization, the graphene is essentially under strain (Supporting Information Figure S1), and the amount of induced stress depends on the simulation details (e.g., initial structure and boundary condition). Because of the strain effect on heat transport in graphene, the uncertainty in the unrelaxed stress can lead to scattered results of the calculated thermal properties.

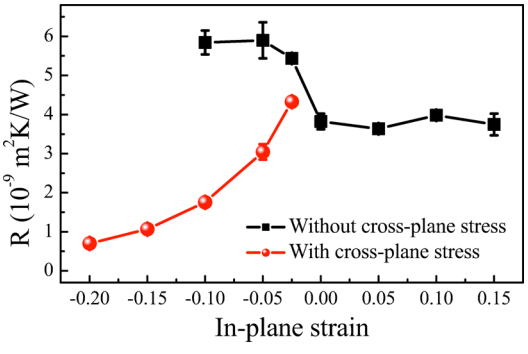

Figure 8. Room temperature Kapitza resistance in few-layer graphene versus in-plane strain. Here the system size is fixed at $N_L = 4$ and $L = 8$ nm.

In summary, we find that FLG can act as a heat conductor or insulator when controlled by strain. Uniaxial cross-plane strain increases the Kapitza resistance monotonically when it varies from compressive to tensile. The tensile in-plane strain has negligible impact on the Kapitza resistance. In contrast, compressive in-plane strain can either increase or reduce Kapitza resistance, depending on the specific way it is applied. We explain these phenomena by analyzing the vibrational spectrum of FLG. Our study demonstrates that both cross-plane and in-plane strain can be used to tune Kapitza resistance in FLG and provides useful guidance toward the design of graphene-based heat dissipation and insulation device by strain engineering.

■ ASSOCIATED CONTENT

Supporting Information

Full simulation details about the strain loading process and the calculations of Kapitza resistance and vibrational density of states are provided. This material is available free of charge via the Internet at http://pubs.acs.org.

■ AUTHOR INFORMATION

Corresponding Author

*E-mail: petros@ethz.ch

Notes

The authors declare no competing financial interest.

■ ACKNOWLEDGMENTS

We acknowledge many helpful discussions with Dr. Panagiotis Angelikopoulos (ETHZ). We are grateful to computing resources from the Brutus Cluster at ETH Zurich and the Swiss National Supercomputing Centre (Project s448). J.C. acknowledges support as an ETH Zurich Fellow.

REFERENCES

(1) Novoselov, K. S.; Geim, A. K.; Morozov, S. V.; Jiang, D.; Zhang, Y.; Dubonos, S. V.; Grigorieva, I. V.; Firsov, A. A. *Science* **2004**, *306*, 666−669.
(2) Zhang, Y.; Tan, Y. -W.; Stormer, H. L.; Kim, P. *Nature* **2005**, *438*, 201−204.
(3) Balandin, A. A. *Nat. Mater.* **2011**, *10*, 569−581.
(4) Pop, E.; Varshney, V.; Roy, A. K. *MRS Bull.* **2012**, *37*, 1273−1281.
(5) Sadeghi, M. M.; Jo, I.; Shi, L. *Proc. Natl. Acad. Sci. U.S.A.* **2013**, *110*, 16321−16326.
(6) Shen, M.; Schelling, P. K.; Keblinski, P. *Phys. Rev. B* **2013**, *88*, 045444.
(7) Balandin, A. A.; Ghosh, S.; Bao, W.; Calizo, I.; Teweldebrhan, D.; Miao, F.; Lau, C. N. *Nano Lett.* **2008**, *8*, 902−907.
(8) Ghosh, S.; Calizo, I.; Teweldebrhan, D.; Pokatilov, E. P.; Nika, D. L.; Balandin, A. A.; Bao, W.; Miao, F.; Lau, C. N. *Appl. Phys. Lett.* **2008**, *92*, 151911.
(9) Cai, W.; Moore, A. L.; Zhu, Y.; Li, X.; Chen, S.; Shi, L.; Ruoff, R. S. *Nano Lett.* **2010**, *10*, 1645−1651.
(10) Xu, X.; Wang, Y.; Zhang, K.; Zhao, X.; Bae S.; Heinrich, M.; Bui, C. T.; Xie, R.; Thong, J. T. L.; Hong, B. H.; Loh, K. P.; Li, B.; Oezyilmaz, B. arXiv: 1012.2937[cond-mat.mes-hall], (accessed Dec 14, 2010).
(11) Ghosh, S.; Bao, W.; Nika, D. L.; Subrina, S.; Pokatilov, E. P.; Lau, C. N.; Balandin, A. A. *Nat. Mater.* **2010**, *9*, 555−558.
(12) Wang, Z.; Xie, R.; Bui, C. T.; Liu, D.; Ni, X.; Li, B.; Thong, J. T. L. *Nano Lett.* **2011**, *11*, 113−118.
(13) Zhong, W.-R.; Zhang, M.-P.; Ai, B.-Q.; Zheng, D.-Q. *Appl. Phys. Lett.* **2011**, *98*, 113107.
(14) Harb, M.; Schmising, C.; von Korff; Enquist, H.; Jurgilaitis, A.; Maximov, I.; Shvets, P. V.; Obraztsov, A. N.; Khakhulin, D.; Wulff, M.; Larsson, J. *Appl. Phys. Lett.* **2012**, *101*, 233108.
(15) Huang, M.; Yan, H.; Heinz, T. F.; Hone, J. *Nano Lett.* **2010**, *10*, 4074−4079.
(16) Choi, S.; Jhi, S.; Son, Y. *Nano Lett.* **2010**, *10*, 3486−3489.
(17) Low, T.; Guinea, F. *Nano Lett.* **2010**, *10*, 3551−3554.
(18) Li, X.; Maute, K.; Dunn, M. L.; Yang, R. *Phys. Rev. B* **2010**, *81*, 245318.
(19) Bonini, N.; Garg, J.; Marzari, N. *Nano Lett.* **2012**, *12*, 2673−2678.
(20) Kitt, A. L.; Qi, Z.; Remi, S.; Park, H. S.; Swan, A. K.; Goldberg, B. B. *Nano Lett.* **2013**, *13*, 2605−2610.
(21) Plimpton, S. *J. Comput. Phys.* **1995**, *117*, 1−19.
(22) Lindsay, L.; Broido, D. A. *Phys. Rev. B* **2010**, *81*, 205441.
(23) Girifalco, L. A.; Hodak, M.; Lee, R. S. *Phys. Rev. B* **2000**, *62*, 13104.
(24) Chen, J.; Zhang, G.; Li, B. *Nanoscale* **2013**, *5*, 532−536.
(25) Wei, Z.; Ni, Z.; Bi, K.; Chen, M.; Chen, Y. *Phys. Lett. A* **2011**, *375*, 1195−1199.
(26) Walther, J. H.; Jaffe, R.; Halicioglu, T.; Koumoutsakos, P. *J. Phys. Chem. B* **2001**, *105*, 9980−9987.
(27) Mao, R.; Kong, B. D.; Kim, K. W.; Jayasekera, T.; Calzolari, A.; Nardelli, M. B. *Appl. Phys. Lett.* **2012**, *101*, 113111.
(28) Frankland, S. J. V.; Harik, V. M.; Odegard, G. M.; Brenner, D. W.; Gates, T. S. *Compos. Sci. Technol.* **2003**, *63*, 1655−1661.
(29) Lee, C.; Wei, X.; Kysar, J. W.; Hone, J. *Science* **2008**, *321*, 385−388.
(30) Balandin, A. A.; Shamsa, M.; Liu, W. L.; Casiraghi, C.; Ferrari, A. C. *Appl. Phys. Lett.* **2008**, *93*, 043115.
(31) Chen, J.; Zhang, G.; Li, B. *J. Appl. Phys.* **2012**, *112*, 064319.
(32) Wang, J.; Zhu, L.; Chen, J.; Li, B.; Thong, J. T. L. *Adv. Mater.* **2013**, *25*, 6884−6888.
(33) Mounet, N.; Marzari, N. *Phys. Rev. B* **2005**, *71*, 205214.
(34) Ferrari, A. C.; Meyer, J. C.; Scardaci, V.; Casiraghi, C.; Lazzeri, M.; Mauri, F.; Piscanec, S.; Jiang, D.; Novoselov, K. S.; Roth, S.; Geim, A. K. *Phys. Rev. Lett.* **2006**, *97*, 187401.
(35) Mohiuddin, T. M. G.; Lombardo, A.; Nair, R. R.; Bonetti, A.; Savini, G.; Jalil, R.; Bonini, N.; Basko, D. M.; Galiotis, C.; Marzari, N.; Novoselov, K. S.; Geim, A. K.; Ferrari, A. C. *Phys. Rev. B* **2009**, *79*, 205433.
(36) Tsoukleri, G.; Parthenios, J.; Papagelis, K.; Jalil, R.; Ferrari, A. C.; Geim, A. K.; Novoselov, K. S.; Galiotis, C. *Small* **2009**, *5*, 2397−2402.
(37) Patton, K. R.; Geller, M. R. *Phys. Rev. B* **2001**, *64*, 155320.
(38) Hu, B.; Yang, L.; Zhang, Y. *Phys. Rev. Lett.* **2005**, *97*, 124302.
(39) Duba, J. C.; English, T. S.; Piekos, E. S.; Soffa, W. A.; Zhigilei, L. V.; Hopkins, P. E. *Phys. Rev. B* **2011**, *84*, 193301.